small methods
www.small-methods.com

A Bio-Inspired Magnetic Soft Robotic Fish for Efficient Solar-Energy Driven Water Purification

Jingjing Qin, Jiahao Li, Guozheng Yang, Kaibin Chu, Leiqian Zhang, Fangping Xu, Yujie Chen, Yaoxin Zhang, Wei Fan, Johan Hofkens, Bo Li, YinBo Zhu, HengAn Wu, Swee Ching Tan, Feili Lai, and Tianxi Liu**

Solar-driven water evaporation is a promising solution for global water scarcity but is still facing challenges due to its substantial energy requirements. Here, a magnetic soft robotic bionic fish is developed by combining magnetic nanoparticles (Fe_3O_4), poly(*N*-isopropylacrylamide), and carboxymethyl chitosan. This bionic fish can release liquid water through hydrophilic/hydrophobic phase transition and dramatically reduce energy consumption. The introduced Fe_3O_4 nanoparticles endow the bionic fish with magnetic actuation capability, allowing for remote operation and recovery. Additionally, the magnetic actuation process accelerates the water absorption rate of the bionic fish as confirmed by the finite element simulations. The results demonstrate that bionic fish can effectively remove not only organic molecular dyes dissolved in water but also harmful microbes and insoluble microparticles from natural lakes. Moreover, the bionic fish maintains a good purification efficiency even after five recycling cycles. Furthermore, the bionic fish possesses other functions, such as salt purification and salt rejection. Finally, the mechanism of water purification is explained in conjunction with molecular dynamics calculations. This work provides a new approach for efficient solar-energy water purification by phase transition behavior in soft robotics.

1. Introduction

With global concerns over population growth and environmental pollution, the scarcity of clean water has emerged as a significant challenge.[1–4] Developing technologies for water purification from wastewater/seawater has gained increasing attention with a focus on achieving cost-effectiveness, low energy consumption, and minimal environmental impact. Although thermal-based water treatments (e.g., multi-effect distillation) are well established, they require massive power consumption and centralized infrastructure.[5,6] Reverse osmosis systems, utilizing membrane-based technology, can reduce energy consumption but still depend on advanced supporting infrastructure and frequent maintenance.[7,8,3] Solar distillation is of great interest due to its superior sustainability and environmental

J. Qin, K. Chu, L. Zhang, F. Xu, W. Fan, T. Liu
The Key Laboratory of Synthetic and Biological Colloids
Ministry of Education
School of Chemical and Material Engineering
International Joint Research Laboratory for Nano Energy Composites
Jiangnan University
Wuxi 214122, P. R. China
E-mail: txliu@jiangnan.edu.cn

J. Li, B. Li, Y. Zhu, H. Wu
CAS Key Laboratory of Mechanical Behavior and Design of Materials
Department of Modern Mechanics
CAS Center for Excellence in Complex System Mechanics
University of Science and Technology of China
Hefei 230027, P. R. China

G. Yang, Y. Chen, F. Lai
State Key Laboratory of Metal Matrix Composites
School of Materials Science and Engineering
Shanghai Jiao Tong University
Shanghai 200240, P. R. China
E-mail: feililai@sjtu.edu.cn, feili.lai@kuleuven.be

Y. Zhang
China-UK Low Carbon College
Shanghai Jiao Tong University
3 Yinlian Road, Shanghai 201306, P. R. China

J. Hofkens, F. Lai
Department of Chemistry
KU Leuven
Celestijnenlaan 200F, Leuven 3001, Belgium

J. Hofkens
Department of Molecular Spectroscopy
Max Planck Institute for Polymer Research
55128 Mainz, Germany

S. C. Tan
Department of Materials Science and Engineering
National University of Singapore
Singapore 117574, Singapore

The ORCID identification number(s) for the author(s) of this article can be found under https://doi.org/10.1002/smtd.202400880

DOI: 10.1002/smtd.202400880

friendliness, outcompeting fossil-based energy resources.[9,10] However, the practical application of solar evaporation and water collection is hindered by the need to overcome the heat of evaporation and the additional energy required for condensing the evaporated water vapor.[11–13] Like all solar energy-driven applications, the approach suffers from intermittence or limited solar energy supply.

Recently, various ingenious approaches have been explored to address the issue of insufficient solar energy supply, such as improving sunlight capture, enhancing solar-to-thermal efficiency, and minimizing heat loss to the surroundings.[14–18] Based on the above strategies, multi-functional hydrogels with wide wavelength bands and high light absorption have developed successively, which ensure rapid increases in their surface temperature, thus contributing to water evaporation and significantly improving the water purification rate. However, the performance of current state-of-the-art hydrogels remains insufficient for practical demands.[19–21] To minimize energy consumption and improve overall efficiency during wastewater treatment, temperature-sensitive hydrogels that can undergo significant volume changes above and below the low critical solution temperature (LCST) have been put forward in the field of solar energy-based water purification.[22] Among them, poly(*N*-isopropylacrylamide) (PNIPAm) hydrogel is a typical one with an LCST of ≈32 °C, which is much lower than the temperature for water evaporation.[23–27] The reversible hydrophilic/hydrophobic switch of PNIPAm hydrogel allows for direct exclusion of liquid water, bypassing the evaporation and condensation processes involved in solar water evaporation. Therefore, it presents a promising avenue for an energy-efficient and effective approach to achieve solar-powered water purification.

However, the existing solar-powered hydrogels for water purification are limited by their inability to move smoothly and adsorb pollutants in specific areas. Particularly, external interventions are necessary to facilitate their migration for location changes. Furthermore, the adsorption mechanism also heavily relies on the diffusion behavior of water molecules within the hydrogel matrix, which brings about additional constraints on their flexibility and efficiency in the context of water purification. The magnetically propelled robotic technique has garnered tremendous interest due to its characteristics of remote and precise control, reusability, biocompatibility, and availability.[28–32] These moving robots demonstrate superior flexibility and shorter processing time than static materials, and allow remote operation control in specific water areas.[33,34] Zhang et al. developed magnetic microrobots that can remove heavy metal ions effectively by utilizing controlled collective motion, resulting in enhanced adsorption capacity and reduced removal times compared to non-mobile counterparts.[35] Therefore, magnetic-driven robots are crucial for addressing water pollution challenges due to their exceptional convenience, remote control capabilities, and enhanced efficiency in advanced recovery applications. Nevertheless, as the polymerization process of PNIPAm hydrogels is relatively slow and the added magnetic particles still present problems, such as easy precipitation and aggregation, there is still room for the development of a suitable method for the preparation of magnetic PNIPAm hydrogels.

Here, a bionic fish-inspired soft robot was prepared successfully by in situ growth of Fe_3O_4 nanoparticles in the cross-linked networks of PNIPAm/carboxymethyl chitosan (CMCS) hydrogel, which can move in different water environments smoothly and quickly due to the uniformly distributed magnetic nanoparticles. Based on the rich functional groups in CMCS (such as —OH, —COOH, and —NH_2), this material exhibits an excellent capability to adsorb various pollutants. Therefore, the bionic fish can also confine various organic dyes within the natural polysaccharide of CMCS (as proved by molecular dynamic simulations) and filter out insoluble particles and harmful microbes from natural lake water due to its 3D network, resulting in the production of abundant clean water when reaching the LCST of PNIPAm. Additionally, the bionic fish also possesses the ability for salt purification and salt rejection, demonstrating its diverse functions in water treatment.

2. Results and Discussion

Figure 1a illustrates the process for water purification of the bionic fish, which can navigate through contaminated water controllably via preset magnetic forces, ultimately absorbing water and acting as an adsorbent until it is fully saturated. Throughout this absorption process, the bionic fish can filter largely sized pollutants (e.g., large suspended particles), while some specific pollutants (e.g., dyes) are adsorbed by the bionic fish and confined in the carboxymethyl chitosan (CMCS) network tightly. After recycling the bionic fish from the polluted water under a magnetic field, they can release abundant clean water through natural exposure to light. When exposed to light, the Fe_3O_4/PNIPAm/CMCS (FPC) hydrogel undergoes a transformation from a hydrophilic state to a hydrophobic state around the LCST of PNIPAm (Figure 1b), facilitating a rapid and efficient release of liquid water from the hydrogel. Figure 1c illustrates the preparation process of the FPC hydrogel. The PNIPAm precursor solution is enriched with a multifunctional group-containing polymer called CMCS.[36] By applying a combination of chemical cross-linking with the cross-linking agent of *N,N'*-methylenebis(acrylamide) (MBA) and physical cross-linking through hydrogen bonding between functional groups, as well as using potassium peroxodisulfate (KPS) as the initiator, the PNIPAm/CMCS hydrogel can be synthesized, ultimately leading to the formation of a monolithic structure. Subsequently, the Fe_3O_4 nanoparticles are deposited in situ into the hydrogel network by co-precipitation, which effectively prevents their aggregation. As depicted in the corresponding scanning electron microscopy (SEM) images in Figure 1d and Figure S1 (Supporting Information), both the FPC-0.5 ("0.5" represents the mass ratio of CMCS to PNIPAm) and PNIPAm/CMCS-0.5 have cellular features with highly porous structures, which can provide abundant spaces and channels for water storage and penetration. As compared to the smooth pore walls of PNIPAm/CMCS-0.5 in Figure S1b (Supporting Information), the pore walls of FPC-0.5 hydrogel become relatively rough without obvious particle aggregation (Figure S2, Supporting Information), which can be attributed to the incorporated Fe_3O_4 nanoparticles. The optical images of the hydrogel shown in Figure S3 (Supporting Information) indicate that the surface and cross-section of the FPC-0.5 hydrogel exhibit a uniform color, which corroborates the macroscopically even distribution of Fe_3O_4 nanoparticles. Energy dispersive spectroscopy (EDS) elemental mapping of FPC-0.5 (Figure 1e) reveals a

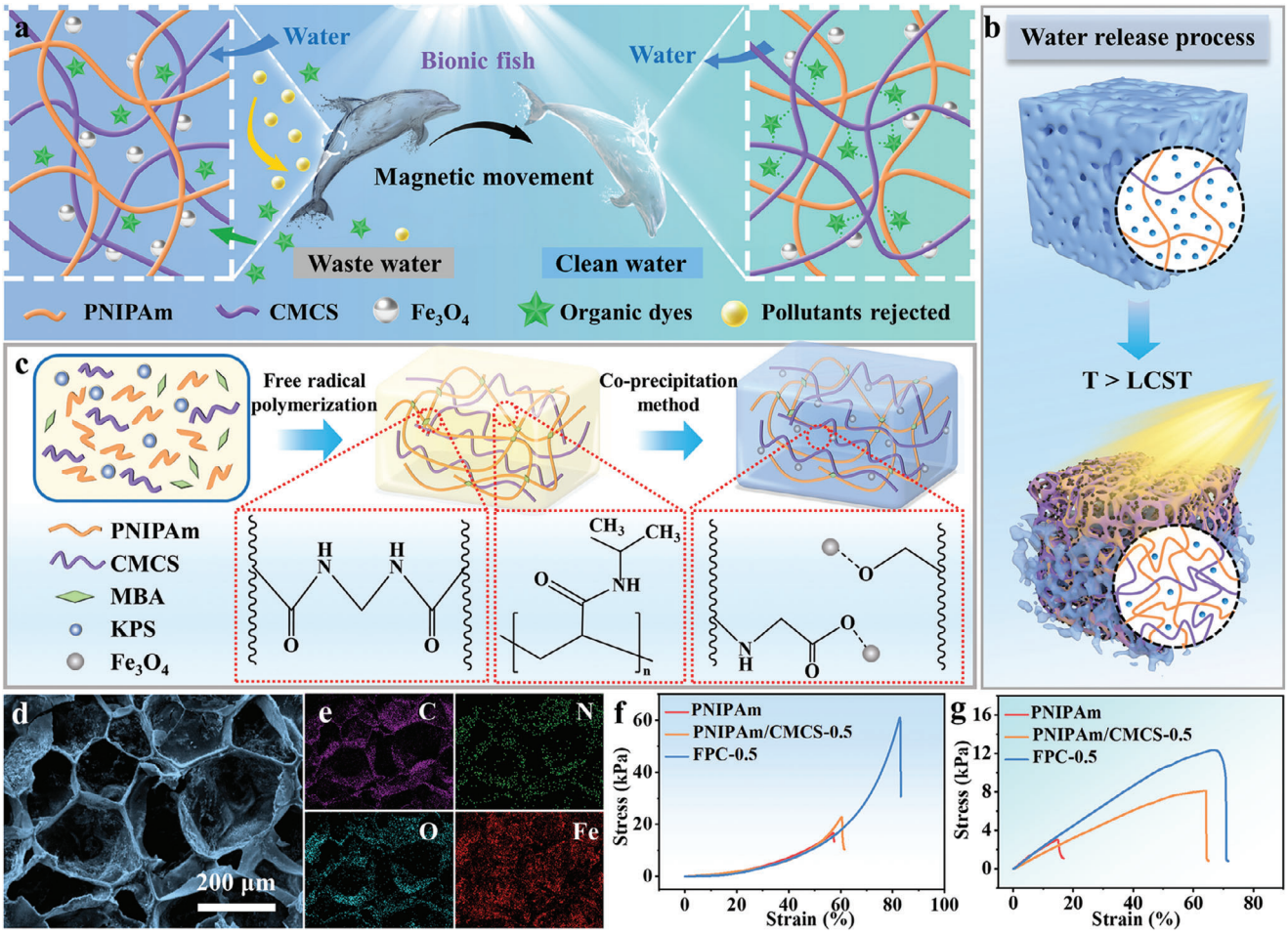

Figure 1. a) Schematic illustration for solar water purification using bionic fish. b) Schematic of the thermally driven water release process in bionic fish. c) Diagram of the fabrication process for FPC hydrogel. d) SEM image and e) corresponding EDS elemental mappings of FPC-0.5. f) Compressive and g) tensile strain-stress curves of the PNIPAm, PNIPAm/CMCS-0.5, and FPC-0.5.

uniform distribution of Fe and demonstrates the homogeneous decoration of Fe_3O_4 nanoparticles within the networks of FPC-0.5. As shown in the X-ray diffraction (XRD) patterns of PNIPAm, CMCS, and FPC-0.5 in Figure S4 (Supporting Information), the peaks at 20° of PNIPAm and CMCS hydrogels originate from their typical polymeric skeletons,[37,38] while the FPC-0.5 hydrogel shows peaks at 35.8°, 43.5°, 57.3°, and 63.0°, which can be assigned to the (311), (400), (511), and (440) planes of Fe_3O_4 (JCPDS No. 75–0449), respectively.[39] It also confirms the incorporation of Fe_3O_4 nanoparticles in the network of FPC hydrogel. The chemical state of Fe in FPC-0.5 was further investigated by X-ray photoelectron spectroscopy (XPS) measurement. In the XPS spectrum of Fe 2p (Figure S5, Supporting Information), the peaks at 712.3 and 725.7 eV belong to Fe $2p_{3/2}$ and Fe $2p_{1/2}$ of Fe^{3+}, and the peaks at 710.0 and 723.7 eV belong to Fe $2p_{3/2}$ and Fe $2p_{1/2}$ of Fe^{2+}, indicating the formation of the Fe_3O_4 in FPC-0.5.[40,41] A key requirement for a practical hydrogel is to have elasticity. As shown in Figure 1f,g, the addition of CMCS results in a slightly increased compression of the PNIPAm/CMCS-0.5 hydrogel from 57% to 61%, while increasing its elongation at break dramatically from 15% to 64%. This is due to the strengthened network structure with abundant hydrogen bonds between CMCS and PNIPAm, resulting in increased compressive strength for PNIPAm/CMCS-0.5. Furthermore, internal friction and rupture of hydrogen bonds within CMCS chains effectively dissipate energy, leading to a significant improvement in elongation at break.[42–44] Additionally, the further incorporated Fe_3O_4 nanoparticles can increase both the compressibility and elongation at breaks of the FPC-0.5 hydrogel to higher values of 83% and 71%, respectively. The reason for that is the homogeneous dispersion of Fe_3O_4 in the hydrogel matrix is beneficial to dispersing the stresses, alleviating the crack propagation, and reducing the stress concentration caused by external force.[45,46] These results jointly demonstrate that CMCS and Fe_3O_4 have positive effects on enhancing the mechanical properties of the FPC-0.5 hydrogel.

Given that the magnetic responsiveness of hydrogels plays a crucial role in controlling their movement and recovery, the magnetic property of the FPC-0.5 was first evaluated with vibrating sample magnetometry. As shown in **Figures** 2a and S6 (Supporting Information), the coercivity and residual magnetization of the FPC-0.5 in the range of −20 to 20 kG are 63.8 G and 2.9 emu g^{-1}, respectively, reflecting the superparamagnetic character of the Fe_3O_4 nanoparticles in the FPC-0.5.[47] By controlling the

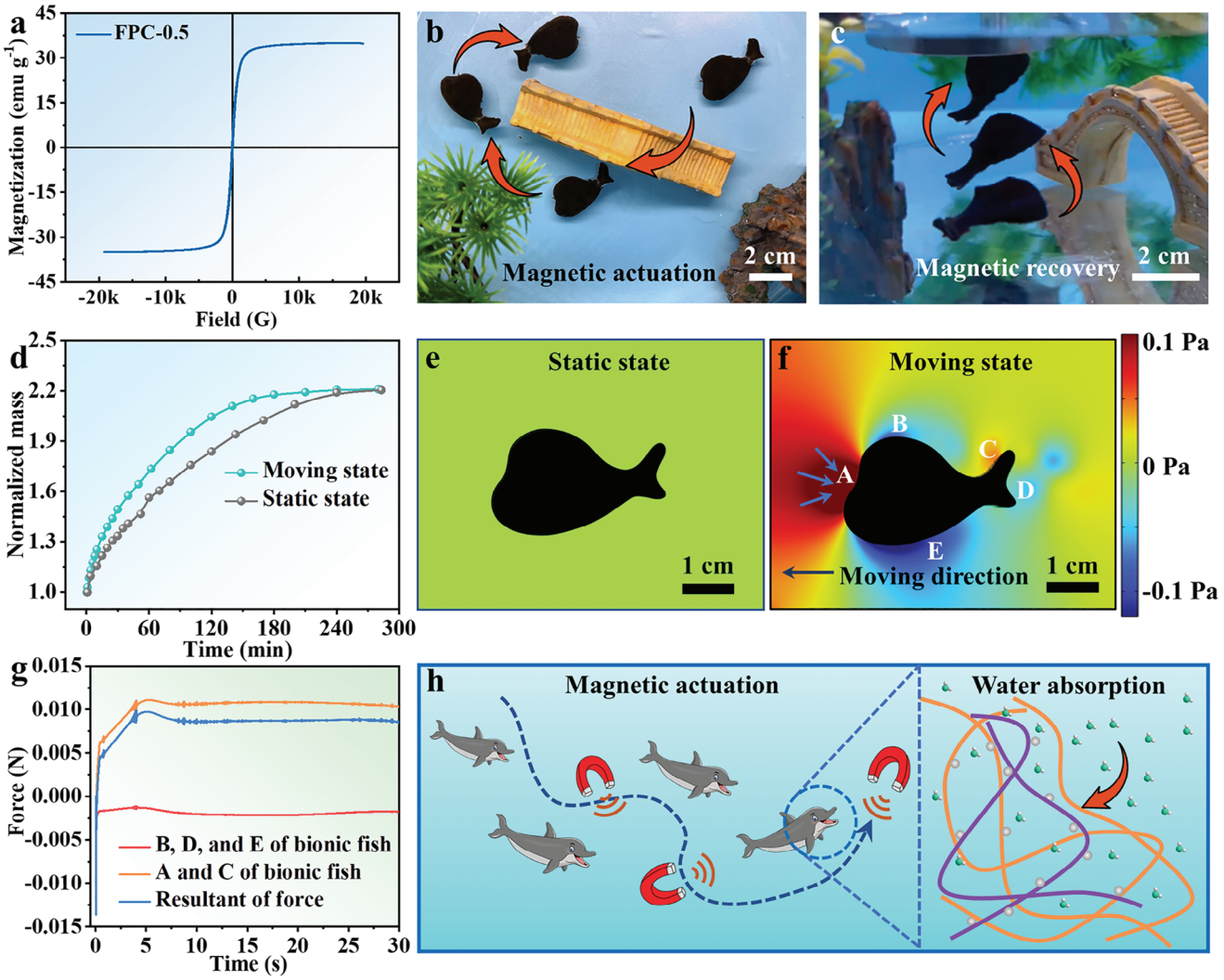

Figure 2. a) Magnetization curve of FPC-0.5. Optical photographs of b) the magnetic-driven process and c) the magnetic recovery process of bionic fish. d) Plots of normalized masses against time for bionic fish during the swelling process in moving and static states. Water pressure distributions of the models e) at static and f) in moving states. g) The curves of the force and time acting on a bionic fish in a moving state. A, B, C, D, and E parts of the bionic fish are labeled in (f). h) A schematic diagram illustrating the magnetic-driven process of the bionic fish and the gel network in its head for water absorption.

magnitude and direction of the magnetic field, the position of the bionic fish (made of FPC-0.5 hydrogel) can be well controlled as shown in Figure 2b and Movie S1 (Supporting Information). This control enables the bionic fish to follow a precise trajectory under the influence of the magnetic field, facilitating its seamless navigation through the bridge hole and subsequent return to the initial position. Figure 2c and Movie S2 (Supporting Information) show the recovery process of the bionic fish, which can be fished out from the water easily by using a magnet. That is to say, the movement of the bionic fish can be controlled to reach the water that needs to be treated, and it can also be recovered through the magnetic field after completing the absorption of polluted water. Interestingly, the water uptake rate of the bionic fish in a moving state is significantly higher than that in a static state (Figure 2d). In this regard, it takes 4 h for bionic fish to achieve complete water absorption under a static state. The adverse water conditions are also simulated using a stirring approach, which conclusively reveals the substantial enhancement in water uptake efficacy of bionic fish, resulting in a shortened saturation time for maximum water absorption capacity (<3 h). In order to investigate the reasons for the above observation, finite element analysis was conducted to simulate the pressure exerted by the liquid on the surface of the hydrogel in both moving and static states (Figure 2e,f). As illustrated in Figure 2e, the bionic fish encounters no discernible pressure while at rest in water, with its swelling process being solely influenced by osmotic pressure. However, the A and C parts of a bionic fish experience higher pressures directed toward its interior than those at other parts in a moving state, which are beneficial for the water penetration into the hydrogel. On the other hand, the B, D, and E regions of the bionic fish experience pressure directed toward the exterior of the material, which may impede the water absorption process.

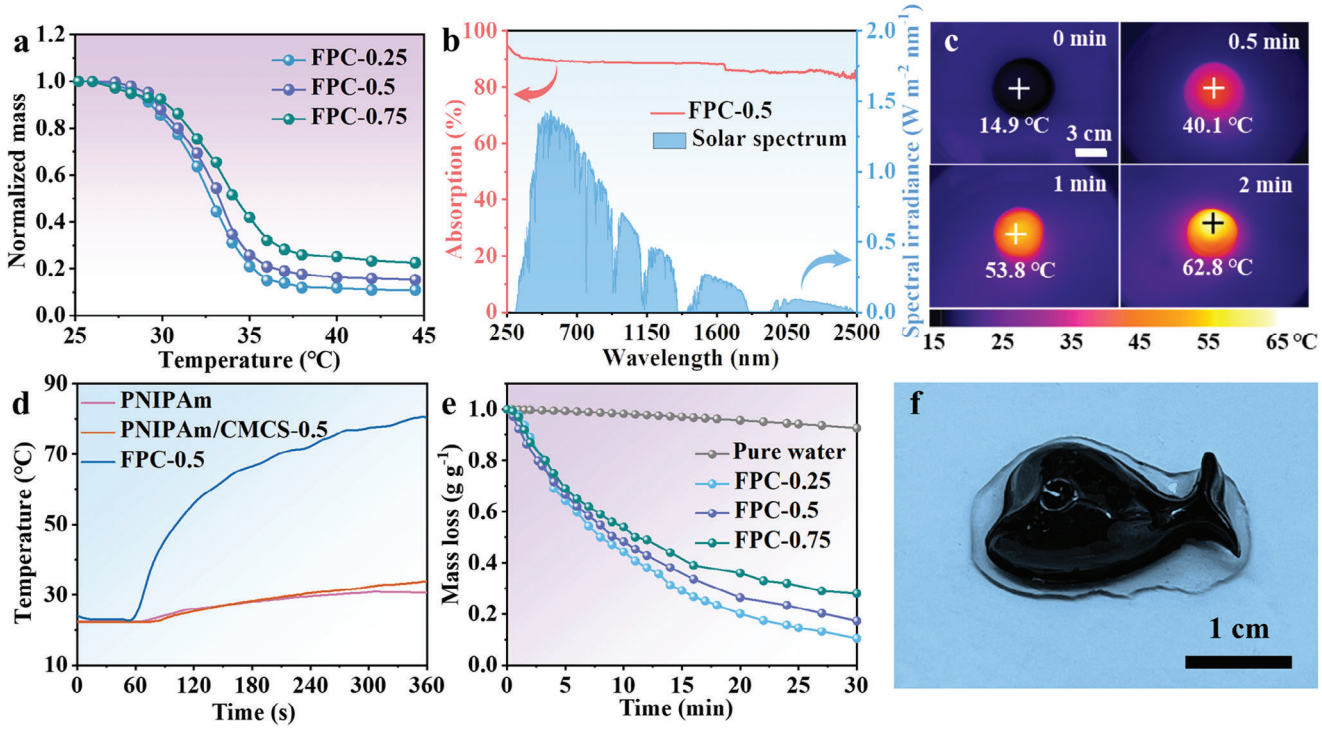

Figure 3. a) Normalized mass curves of FPC-0.25, FPC-0.5, and FPC-0.75 with increasing temperature. b) UV–Vis–NIR spectrum of FPC-0.5 and the normalized spectral solar irradiance density of air mass 1.5 global (AM 1.5 G) tilt solar spectrum. c) IR images of FPC-0.5 under xenon lamp irradiation at different times. d) Surface temperature changes of PNIPAm, PNIPAm/CMCS-0.5, and FPC-0.5 hydrogels by thermocouple under xenon lamp illumination. e) The mass change of pure water, FPC-0.25, FPC-0.5, and FPC-0.75 under xenon lamp irradiation. f) Photograph of bionic fish under xenon lamp irradiation for 10 min.

To demonstrate that the dominant pressure during motion is directed toward the interior of the hydrogel, an integration analysis of the surface pressure was performed. As shown in Figure 2g, when the bionic fish is moving, the positive force of A and C of bionic fish, as well as the negative force of B, D, and E of bionic fish, are calculated separately, and their resultant of force is still positive, indicating that the water exerts a force inside the structure of the bionic fish. The results depicted in Figure S7 (Supporting Information) illustrate a correlation between the force and the movement speed of the bionic fish, the higher the movement speed is, the stronger the force becomes. Consequently, this motion facilitates accelerated water into the bionic fish, thereby expediting the water treatment process. Figure 2h shows a schematic for the movement of the bionic fish. By manipulating the magnetic field precisely, the bionic fish can move and recover in the water accurately. In the moving state, the bionic fish is able to absorb water at an increased rate, especially at its head, which is beneficial for the entrance of water into the hydrogel, thus accelerating the water purification process.

The solar-induced phase change of FPC plays a vital role in the rapid release of water, enabling the production of clean water. This hydrophilic/hydrophobic phase transition phenomenon of FPC hydrogels is confirmed by the substantial reduction in their masses as the temperature increases. The mass curves of various FPC hydrogels reveal that their LCST values are at ≈32 °C (**Figure** 3a), which are according to the LCST of PNIPAm,[23,48] suggesting that the incorporation of CMCS and Fe_3O_4 nanoparticles has negligible effect on the LCST of the hydrogels. For the evaluation of the solar absorbance of FPC-0.5, UV–Vis–NIR spectroscopy was recorded across the wavelength range from 250 to 2500 nm. As shown in Figure 3b, the FPC-0.5 demonstrates an efficient light absorption in the wavelength range of 250–2500 nm, which serves as the foundation for its notable photothermal conversion efficacy. Under a 300 W xenon lamp as the light source to simulate solar radiation, the surface temperature distributions of the FPC-0.5 hydrogel were captured at specific time intervals (0, 0.5, 1, and 2 min) using an infrared thermographic camera. As the corresponding images are shown in Figure 3c, the FPC-0.5 displays an excellent ability for light conversion into heat, leading to its rapid temperature increase to 62.8 °C within 2 min. Additionally, the surface temperature variation was also recorded using a thermocouple. The surface temperature of FPC-0.5 increases rapidly and is stabilized at ≈80 °C, while the temperatures of PNIPAm/CMCS-0.5 and PNIPAm hydrogels keep below 32 °C under xenon lamp illumination for 5 min (Figure 3d), suggesting that the rapidly increased surface temperature of FPC-0.5 can be assigned to the presence of Fe_3O_4 nanoparticles with excellent abilities in absorbing light and photothermal conversion.[49] Therefore, the unique composite structure of FPC-0.5 provides the possibility to reach the phase transition temperature rapidly. As shown in Figure 3e, the mass loss of water-swollen FPC under irradiation exhibits a time-dependent increase. Specifically, the mass loss of FPC-0.5 reaches a high value of 82.7% after 30 min of illumination. With the increase of CMCS content in

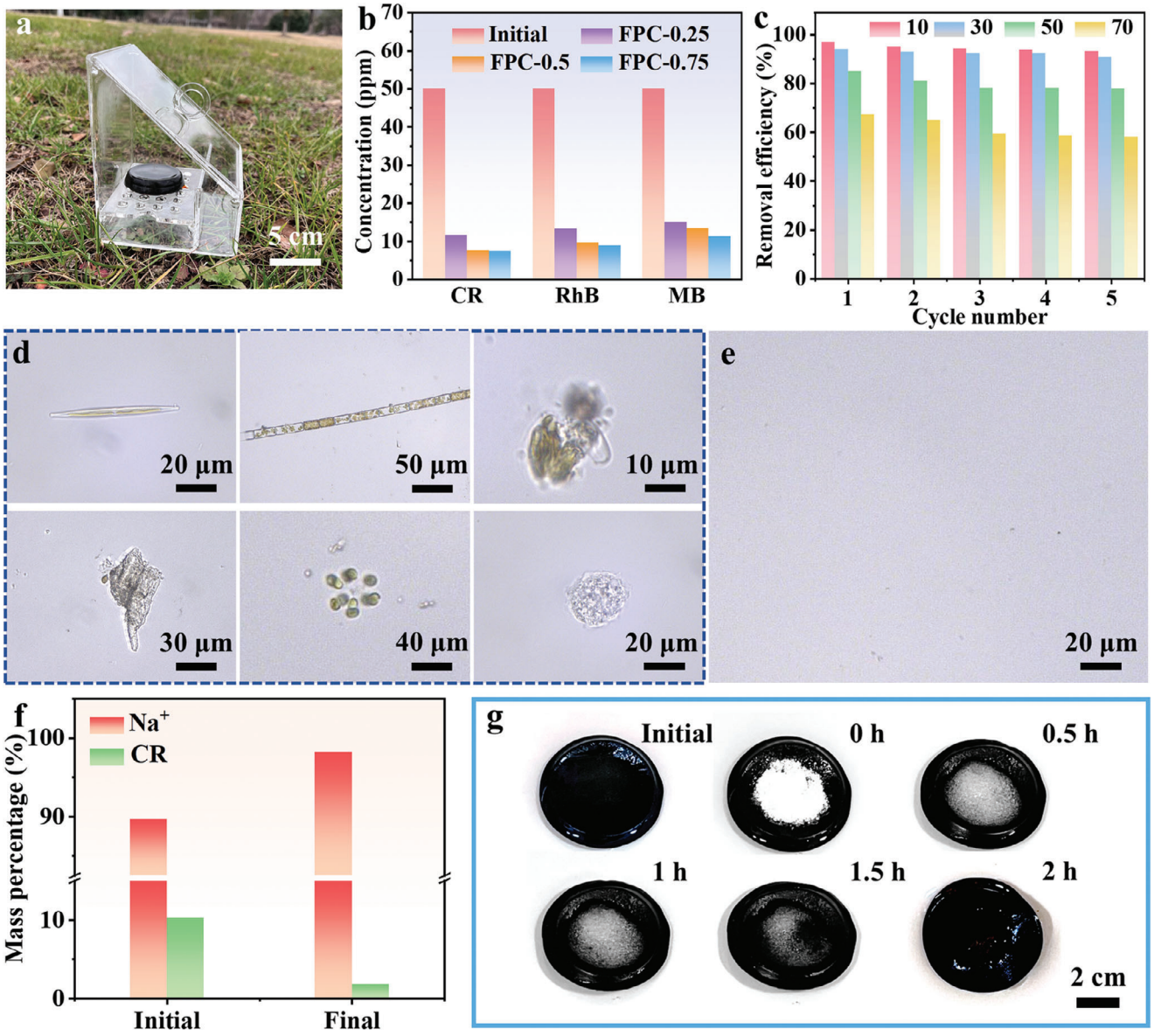

Figure 4. a) photograph of the solar-powered water purification device. b) The residues of CR, MB, and RhB in purified water using FPC-0.25, FPC-0.5, and FPC-0.75 hydrogels. c) Cycling performance of FPC-0.5 in purifying CR solutions at different concentrations (10, 30, 50, and 70 ppm). Optical images of d) natural lake water e) and purified lake water by FPC-0.5. f) Mass percentages of Na^+ and CR before and after purifications with FPC-0.5 hydrogel. g) Optical images showing the salt rejection capability of the FPC-0.5 hydrogel.

FPC hydrogel from 0.25 to 0.75, a corresponding reduction in the mass loss of the hydrogel can be observed from 89.5% to 72.0%, which arises from the impediment caused by an excessive amount of CMCS on the phase transition process. Figure 3f shows a photograph of the bionic fish with a large amount of discharged water after 10 min illumination. This can be attributed to the excellent photothermal conversion of Fe_3O_4 nanoparticles in the hydrogel upon exposure to light. The subsequent increase in hydrogel temperature (>32 °C) induces a shrinkage of the hydrogel network, resulting in the drainage of water from the hydrogel.

A logical and crucial method for obtaining clean water is through the purification of water obtained from a contaminated source. In order to evaluate the purification ability of the hydrogel, FPC was put into sewage wastewater and controlled for directed movement by a magnetic field. After sufficient water absorption, the FPC can be recovered easily by using a magnetic field and put into the solar water purification device for pure water release (**Figure** 4a). When the hydrogel is placed on the platform (in the middle of the device) and exposed to light illumination, the surface temperature of the hydrogel rises rapidly and undergoes a phase transition, causing the water loss of the hydrogel. The released clean water from the hydrogel can converge to the bottom of the device through the holes in the platform. In addition, a small portion of the water condenses into droplets at the top of the container, which can also slide along the

sloping walls of the container into the bottom slot. In this way, clean water can be collected efficiently. The purification effect of FPC on small molecule dyes, such as congo red (CR), methylene blue (MB), and rhodamine B (RhB), was investigated at initial concentrations of 50 ppm. To elucidate the specific role of Fe_3O_4 in the water purification process, several FPC-0.5 samples with varying Fe_3O_4 contents were synthesized by adjusting the concentrations of Fe^{2+} and Fe^{3+} solutions. The thermogravimetric analysis (TGA) curves of FPC-0.5 hydrogels illustrated in Figure S8 (Supporting Information), indicate that the mass fractions of Fe_3O_4 in different FPC-0.5 hydrogels are 10.0%, 21.1%, 24.1%, and 24.7%, respectively. The Fe_3O_4 content in the FPC-0.5 hydrogel synthesized with Fe^{2+} and Fe^{3+} concentrations of 0.2 and 0.4 M is 24.7%. This value is similar to the FPC-0.5 hydrogel obtained using Fe^{2+} and Fe^{3+} concentrations of 0.15 and 0.3 M, suggesting that the Fe_3O_4 content in the FPC-0.5 hydrogel produced by this method has reached its maximum. Subsequently, the CR removal efficiencies of these FPC-0.5 hydrogels were analyzed. As shown in Figure S9 (Supporting Information), the PNIPAm/CMCS-0.5 hydrogel without Fe_3O_4 content achieves a CR removal efficiency of 79.6%, underscoring the critical role of CMCS in the purification process. With the gradual increase in Fe_3O_4 content, the water purification efficiency of the hydrogel improves slightly, rising from 79.6% to 85.6%. However, the contribution of Fe_3O_4 nanoparticles to the water purification process is relatively limited. To ensure optimal magnetic driving capabilities, a high Fe_3O_4 loading amount of 21.1 wt.% was selected, and the purification ability of FPC-0.5 hydrogels with different CMCS contents was also analyzed subsequently. As shown in Figure 4b, the contents of CR, MB, and RhB in the contaminative solutions are reduced significantly after the purification treatment by using FPC-0.25, FPC-0.5, and FPC-0.75 hydrogels. By taking a CR solution as an example, the concentrations of CR after the purification treatment with FPC-0.25, FPC-0.5, and FPC-0.75 are 11.5, 7.7, and 7.5 ppm, respectively. Note that an increase in CMCS content results in reducing the water loss during the phase transition, subsequently resulting in a reduced quantity of purified water (Figure 3a). Conversely, an insufficient CMCS content would decrease the dye removal efficiency of the FPC hydrogel. Based on these points, FPC-0.5 emerges as the optimal composition with enhanced water purification volume and removal efficiency. Moreover, the water purification capability of FPC-0.5 is influenced by various factors, such as pH value and initial concentration of the dye. As shown in Figure S10a (Supporting Information), the removal efficiency of CR, MB, and RhB from aqueous solutions is highly dependent on the pH value of the solution as the FPC-0.5 hydrogel undergoes deprotonation under a high pH value. At higher pH values, the surface of FPC-0.5 becomes negatively charged due to the presence of carboxylate groups (-COO^-), which can provide more adsorption sites for cationic dyes of MB and RhB.[50] In acidic conditions, the increased H^+ concentration causes dramatically protonated -NH_2 groups in CMCS and leads to a positively charged surface on FPC-0.5 for its strong interaction with anionic dye molecules.[51] Figure S10b (Supporting Information) shows that the dye removal efficiency of the FPC-0.5 hydrogel is closely related to the concentration of dye solution. As the dye concentration increases from 10 to 70 ppm, the dye removal efficiency decreases significantly. This decline occurs as the dye content in FPC-0.5 hydrogel has reached to its maximum adsorption capacity. Additionally, the FPC-0.5 still maintains an excellent purification ability of the CR-contained solution after five recycling cycles (Figure 4c), demonstrating its potential for practical application. Considering that the bionic fish is controlled by a magnetic field during dye adsorption, the effect of the magnetic field on dye removal efficiency was also analyzed. As shown in Figure S11 (Supporting Information), the water purification efficiencies of the bionic fish are similar in both static and moving states, suggesting that the magnetic field has no significant effect on the water purification capability of the bionic fish. Natural water from lakes (Figure S12, Supporting Information) is a typical water source in daily life, while it is full of different kinds of harmful microbes in specific seasons (Figure 4d) and insoluble microparticles (e.g., microplastics and suspended sediment particles). The purification ability of the FPC-0.5 hydrogel was further evaluated by immersing it in the water and "catching" it magnetically after sufficient water absorption. The blank image of the treated lake water (Figure 4e) demonstrates the positive role of FPC-0.5 hydrogel in filtering harmful microbes and insoluble microparticles. Based on the high adsorption capacity of the FPC hydrogel, the function of FPC hydrogel to purify salt (e.g., NaCl) was also investigated by mixing NaCl with CR (an example of an organic pollutant in water). As shown in Figure 4f, the mass percentages of Na^+ and CR are 90% and 10%, respectively, where the mass percentage refers to the proportion of the solute mass to the total solute mass. After the treatment with the FPC-0.5 hydrogel, an increase in the mass fraction of Na^+ to 98% is observed with the corresponding photographs of the NaCl solutions before and after purification shown in Figure S13 (Supporting Information). This result unequivocally demonstrates the efficient removal of certain pollutants from seawater by the FPC-0.5 hydrogel, validating its application in the salt purification process. Salt rejection is another important aspect of long-term solar purification of salt solutions. Figure 4g illustrates the salt rejection properties of FPC hydrogel, where a large amount of salt is deposited on the top surface of the hydrogel at 0 h. The deposited salts are dissolved by the water molecules delivered from the hydrogel rapidly and disappear within 2 h completely. This observation strongly demonstrates the ability of the FPC hydrogel to reject salt effectively, which also shows that the FPC hydrogel has significant anti-fouling and self-cleaning properties.

The mechanism for water purification of FPC hydrogel was also revealed from a molecular perspective by molecular dynamics (MD), where CR is regarded as a target molecule (Figure S14, Supporting Information). The hydrophobic effect of PNIPAm/CMCS is analyzed by the radius of gyration (R_g) of PNIPAm and radial distribution functions (RDFs) of C—C between CH_3 groups of the isopropyl moiety in the side-group of PNIPAm at 290 and 350 K. Generally, R_g provides a method to quantify the conformation of the polymer chains. The R_g of the PNIPAm chain decreases from 17.1 to 14.0 Å when the temperature increases from 290 to 350 K (Figure S15, Supporting Information), indicating that the majority of PNIPAm chains would collapse at a higher temperature. The RDFs of C-C between CH_3 groups in Figure S16 (Supporting Information) exhibit a higher value at 350 K than that at 290 K. This temperature dependence is in agreement with the estimation of the transition temperature based on the R_g. The PNIPAm chain is in a coiled state and

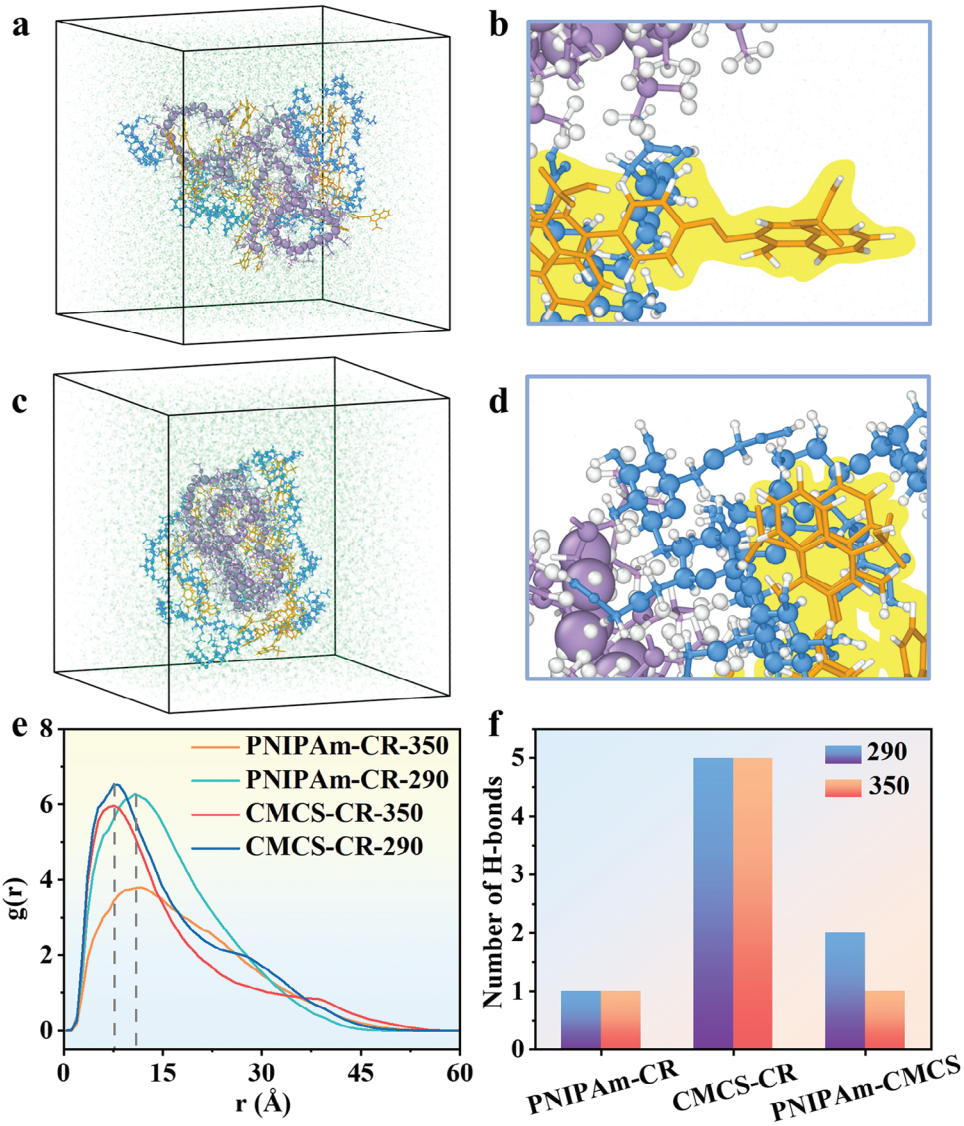

Figure 5. Snapshots of PNIPAm/CMCS system after equilibration at a,b) 290 K and c,d) 350 K over 35 ns, where (b) and (d) are localized enlargements of (a) and (c), respectively. Here, PNIPAm is depicted in purple, CMCS is depicted in blue, CR molecules are depicted in orange, water is shown in green, and all the hydrogen atoms are depicted in white. e) RDFs of CR, PNIPAm, and CMCS obtained from the MD simulations under different temperatures (290 and 350 K). f) Number of hydrogen bonds in equilibrated PNIPAm/CMCS system at 290 and 350 K.

intertwined with the CMCS molecules in 290 K (**Figure** 5a,b), where the CR molecules are adsorbed near the CMCS chains. When the temperature increases to 350 K, the coiled PNIPAm loses abundant H_2O molecules and changes into a globule state, while the CR molecules are still adsorbed near the CMCS chains (Figure 5c,d). Furthermore, RDFs, an essential means of understanding how molecules interact with each other, are computed to predict the phase of trapped CR in a stabilized model. As shown in Figure 5e, as the temperature increases from 290 to 350 K, the first peaks observed between PNIPAm and CR remain consistent at a distance of 10.8 Å without obvious change. However, the intensity of the first peaks of PNIPAm and CR decreases notably (from 6.3 to 3.8 Å) as the temperature increases from 290 to 350 K, which can be attributed to the phase transition occurring in the PNIPAm chains. The distance corresponding to the first peak between CMCS and CR is 7.6 Å at 290 K, which is smaller than the distance corresponding to the peak between PNIPAm and CR, suggesting that CR adsorbs to CMCS rather than PNIPAm. Meanwhile, the first peak between CMCS and CR decreases only slightly (from 6.5 to 6.0) as the temperature changes from 290 to 350 K, indicating that the adsorption between CMCS and CR remains relatively stable and is not appreciably affected by the increased temperature. From the statistical graph of the number of hydrogen bonds (Figure 5f), the number of hydrogen bonds between CMCS and CR is five times the number of hydrogen bonds between PNIPAm and CR at both 290 and 350 K, which proves the efficient interaction force between CR and CMCS once again. The number of hydrogen bonds between PNIPAm and CMCS decreases from 2 to 1 when the temperature changes from 290 to 350 K, which is mainly attributed to

the collapsed structure of PNIPAm. The above results elucidate the mechanism of water purification by FPC based on the porous structure of the hydrogel: the pollutants with large sizes (e.g., microbes) in the water will be filtered out directly; the pollutants with small sizes will diffuse into the interior of the hydrogel and be adsorbed onto the CMCS chains. When the surface temperature of the hydrogel rises above the LCST under illumination, the hydrogel undergoes a phase transition from a hydrophilic state to a hydrophobic state with the loss of confined water from the hydrogel. Since the contaminants can be still adsorbed near the CMCS during this process, clean water can be produced and collected successfully.

3. Conclusion

In summary, a novel design was implemented to develop a hydrogel-based "bionic fish" capable of solar energy absorption through in situ deposition of Fe_3O_4 magnetic nanoparticles. Benefiting from the magnetic properties, the PNIPAm/CMCS fish-shaped hydrogel can move through water following magnetic fields, mimicking swimming motion. The gels can be recovered magnetically as well, after efficient water adsorption in pollutant water bodies. Remarkably, the hydrogel can reach to temperature of its phase change easily via solar irradiation, facilitating rapid water release with minimal energy consumption during the water collection process. The results show that the bionic fish possesses an excellent ability to remove dyes from water (as confirmed by molecular dynamic simulations), as well as filter out harmful microbes and insoluble particles from natural lake water, along with notable reusability. Furthermore, the bionic fish demonstrates remarkable efficacy in salt purification and salt resistance. This innovative approach unveils a promising pathway to achieve highly efficient water purification by introducing phase transition behavior in soft robotic materials.

Supporting Information

Supporting Information is available from the Wiley Online Library or from the author.

Acknowledgements

J.Q. and J.L. contributed equally to this work. The authors sincerely acknowledge financial support from the National Natural Science Foundation of China (52303151, 12172346, 52161135302, and 52211530489), National Key Research and Development Program of China (2022YFB3805700), the Research Foundation Flanders (1298323N and V404923N), and the Program of the Shanghai Academic Research Leader (17XD1400100), and the Youth Innovation Promotion Association CAS (2022465). The authors also thank the characterizations supported by Central Laboratory, School of Chemical and Material Engineering, Jiangnan University. J.H. thanks the Max Planck as a fellow.

Conflict of Interest

The authors declare no conflict of interest.

Data Availability Statement

The data that support the findings of this study are available from the corresponding author upon reasonable request.

Keywords

magnetically responsive hydrogel, PNIPAm, smart materials, solar water purification

Received: June 13, 2024
Revised: September 30, 2024
Published online:

[1] B. Sengupta, Q. Dong, R. Khadka, D. K. Behera, R. Yang, J. Liu, J. Jiang, P. Keblinski, G. Belfort, M. Yu, *Science* **2023**, *381*, 1098.
[2] R. Das, T. Lindström, P. R. Sharma, K. Chi, B. S. Hsiao, *Chem. Rev.* **2022**, *122*, 8936.
[3] R. Ou, H. Zhang, V. X. Truong, L. Zhang, H. M. Hegab, L. Han, J. Hou, X. Zhang, A. Deletic, L. Jiang, G. P. Simon, H. Wang, *Nat. Sustain.* **2020**, *3*, 1052.
[4] J. Li, X. Wang, Z. Lin, N. Xu, X. Li, J. Liang, W. Zhao, R. Lin, B. Zhu, G. Liu, L. Zhou, S. Zhu, J. Zhu, *Joule* **2020**, *4*, 928.
[5] X. Zhou, H. Lu, F. Zhao, G. Yu, *ACS Materials Lett.* **2020**, *2*, 671.
[6] M. Alsehli, J.-K. Choi, M. Aljuhan, *Sol. Energy* **2017**, *153*, 348.
[7] Y. Guo, X. Zhao, F. Zhao, Z. Jiao, X. Zhou, G. Yu, *Energy Environ. Sci.* **2020**, *13*, 2087.
[8] L. Li, N. He, B. Jiang, K. Yu, Q. Zhang, H. Zhang, D. Tang, Y. Song, *Adv. Funct. Mater.* **2021**, *31*, 2104380.
[9] F. Zhao, Y. Guo, X. Zhou, W. Shi, G. Yu, *Nat. Rev. Mater.* **2020**, *5*, 388.
[10] J. Zhao, Z. Liu, S. C. Low, Z. Xu, S. H. Tan, *Adv. Fiber Mater.* **2023**, *5*, 1318.
[11] L. Wu, Z. Dong, Z. Cai, T. Ganapathy, N. X. Fang, C. Li, C. Yu, Y. Zhang, Y. Song, *Nat. Commun.* **2020**, *11*, 521.
[12] X. Su, D. Hao, M. Sun, T. Wei, D. Xu, X. Ai, X. Guo, T. Zhao, L. Jiang, *Adv. Funct. Mater.* **2022**, *32*, 2108135.
[13] Y. Yang, R. Zhao, T. Zhang, K. Zhao, P. Xiao, Y. Ma, P. M. Ajayan, G. Shi, Y. Chen, *ACS Nano* **2018**, *12*, 829.
[14] F. Li, N. Li, S. Wang, L. Qiao, L. Yu, P. Murto, X. Xu, *Adv. Funct. Mater.* **2021**, *31*, 2104464.
[15] Y. Guo, H. Lu, F. Zhao, X. Zhou, W. Shi, G. Yu, *Adv. Mater.* **2020**, *32*, 1907061.
[16] L. Pu, H. Ma, J. Dong, C. Zhang, F. Lai, G. He, P. Ma, W. Dong, Y. Huang, T. Liu, *Nano Lett.* **2022**, *22*, 4560.
[17] P. Tao, G. Ni, C. Song, W. Shang, J. Wu, J. Zhu, G. Chen, T. Deng, *Nat. Energy* **2018**, *3*, 1031.
[18] X. Zhang, J. Liu, W. Li, C. Li, F.-Z. Jiao, Z.-Z. Yu, X. Li, *Compos. Commun.* **2023**, *44*, 101746.
[19] Y. Guo, L. S. Vasconcelos, N. Manohar, J. Geng, K. P. Johnston, G. Yu, *Angew.Chem.Int. Ed.* **2022**, *61*, e202114074.
[20] F. Zhao, X. Zhou, Y. Shi, X. Qian, M. Alexander, X. Zhao, S. Mendez, R. Yang, L. Qu, G. Yu, *Nat. Nanotechnol.* **2018**, *13*, 489.
[21] Z. Wang, X. Wu, F. He, S. Peng, Y. Li, *Adv. Funct. Mater.* **2021**, *31*, 2011114.
[22] Y. Guo, J. Bae, Z. Fang, P. Li, F. Zhao, G. Yu, *Chem. Rev.* **2020**, *120*, 7642.
[23] M. Hua, S. Wu, Y. Ma, Y. Zhao, Z. Chen, I. Frenkel, J. Strzalka, H. Zhou, X. Zhu, X. He, *Nature* **2021**, *590*, 594.
[24] X. Xia, J. Meng, J. Qin, G. Yang, P. Xuan, Y. Huang, W. Fan, Y. Gu, F. Lai, T. Liu, *ACS Appl. Polym. Mater.* **2024**, *6*, 3170.
[25] J. Qin, K. Chu, Y. Huang, X. Zhu, J. Hofkens, G. He, I. P. Parkin, F. Lai, T. Liu, *Energy Environ. Sci.* **2021**, *14*, 3931.
[26] J. Qin, J. Li, K. Chu, G. Yang, L. Zhang, X. Xia, P. Xuan, X. Chen, B. Weng, H. Huang, Y. Chen, W. Fan, Y. Zhu, H. Wu, F. Lai, T. Liu, *Adv. Funct. Mater.* **2023**, *34*, 2311214.
[27] T. Yang, J. Xu, X. Zhang, Y. Liu, P. Ma, *Compos. Commun.* **2024**, *45*, 101789.

[28] X.-Z. Chen, M. Hoop, F. Mushtaq, E. Siringil, C. Hu, B. J. Nelson, S. Pané, *Appl. Mater. Today* **2017**, *9*, 37.
[29] P. Fischer, A. Ghosh, *Nanoscale* **2011**, *3*, 557.
[30] Q. Ze, S. Wu, J. Dai, S. Leanza, G. Ikeda, P. C. Yang, G. Iaccarino, R. R. Zhao, *Nat. Commun.* **2022**, *13*, 3118.
[31] Z. Wang, D. Fu, D. Xie, S. Fu, J. Wu, S. Wang, F. Wang, Y. Ye, Y. Tu, F. Peng, *Adv. Funct. Mater.* **2021**, *31*, 2101648.
[32] J. Tang, C. Yao, Z. Gu, S. Jung, D. Luo, D. Yang, *Angew. Chem., Int. Ed.* **2020**, *59*, 2490.
[33] H. Wang, M. G. Potroz, J. A. Jackman, B. Khezri, T. Maric´, N.-J. Cho, M. Pumera, *Adv. Funct. Mater.* **2017**, *27*, 1702338.
[34] H. Wang, B. Khezri, M. Pumera, *Chem* **2016**, *1*, 473.
[35] Y. Zhang, K. Yan, F. Ji, L. Zhang, *Adv. Funct. Mater.* **2018**, *28*, 1806340.
[36] L. Wang, A. Wang, *Bioresource Technol.* **2008**, *99*, 1403.
[37] C. S. Biswas, A. Biswas, M. Galluzzi, M. I. Shekh, Q. Wang, B. Ray, P. Maiti, F. J. Stadler, *Polymer* **2020**, *203*, 122760.
[38] X. Hu, L. Yan, Y. Wang, M. Xu, *Chem. Eng. J.* **2020**, *388*, 124189.
[39] Y. Mao, Y. Li, F. Zang, H. Yu, S. Yan, Q. Song, Z. Qin, J. Sun, B. C., X. Huang, N. Gu, *Sci. China Mater.* **2022**, *65*, 1646.
[40] X. Fan, L. Xie, J. Liang, Y. Ren, L. Zhang, L. Yue, T. Li, Y. Luo, N. Li, B. Tang, Y. Liu, S. Gao, A. A. Alshehri, Q. Liu, Q. Kong, X. Sun, *Nano Res.* **2022**, *15*, 3050.
[41] S. Li, K. Dong, M. Cai, X. Li, X. Chen, *eScience* **2024**, *4*, 100208.
[42] Y. Yang, X. Wang, F. Yang, H. Shen, D. Wu, *Adv. Mater.* **2016**, *28*, 7178.
[43] R. Zeng, S. Lu, C. Qi, L. Jin, J. Xu, Z. Dong, C. Lei, *J. Appl. Polym. Sci.* **2022**, *139*, e51993.
[44] H. Ding, J. Liu, P. Huo, R. Ding, X. Shen, H. Mao, Y. Wen, H. Li, Z. L. Wu, *Int. J. Biol. Macromol.* **2023**, *253*, 127146.
[45] J. H. Lee, W. J. Han, H. S. Jang, H. J. Choi, *Sci. Rep.* **2019**, *9*, 15024.
[46] X. Zeng, Z. Sun, H. Wang, Q. Wang, Y. Yang, *Compos Sci. Technol.* **2016**, *122*, 149.
[47] D. Liu, Y. Xiao, K.-K. Yang, Y.-Z. Wang, *Compos. Commun.* **2024**, *49*, 101959.
[48] S. Diao, L. Meng, C. M. Pelicano, J. Huang, Z. Tian, F. Lai, T. Liu, S. Cao, *ACS Appl. Mater. Interfaces* **2024**, *16*, 44067.
[49] C. Chen, Z. Huang, L.-A. Shi, Y. Jiao, S. Zhu, J. Li, Y. Hu, J. Chu, D. Wu, L. Jiang, *Adv. Funct. Mater.* **2019**, *29*, 1904766.
[50] Q. Yang, H. Song, Y. Li, Z. Pan, M. Dong, F. Chen, Z. Chen, *J. Mol. Liq.* **2017**, *234*, 18.
[51] C. Lei, F. Wen, J. Chen, W. Chen, Y. Huang, B. Wang, *Polymer* **2021**, *213*, 123316.